



Revisiting the thermal decomposition mechanism of MAPbI₃†

Cite this: DOI: 10.1039/d4cp01318b

 Weijie Yang,^{id abc} Ruiyang Shi,^{abc} Huan Lu,^{abc} Kailong Liu,^{abc} Qingqi Yan,^{abc} Yang Bai,^{abc} Xunlei Ding,^{id de} Hao Li^{id *f} and Zhengyang Gao^{*abc}

The thermal stability of MAPbI₃ poses a challenge for the industry. To overcome this limitation, a thorough investigation of MAPbI₃ is necessary. In this work, thermal gravimetric analysis (TGA) and Fourier transform infrared (FTIR) spectroscopy were conducted to identify the thermal decomposition products of MAPbI₃, which were found to be CH₃I, NH₃, and PbI₂. *In situ* X-ray diffraction (XRD) measurements were then performed in the temperature range from 300 to 700 K, which revealed the significant decomposition of the (110), (220), and (310) surfaces of MAPbI₃ between 550 and 600 K. Density functional theory (DFT) calculations demonstrated that the (220) surface exhibited the highest stability. Additionally, the transition states of thermal decomposition showed that the energy barrier for the decomposition of the (110) surface was 2.07 eV. Our combined experimental and theoretical results provide a better understanding of the thermal decomposition mechanism of MAPbI₃, providing valuable theoretical support for the design of long-term stable devices.

 Received 29th March 2024,
 Accepted 5th June 2024

DOI: 10.1039/d4cp01318b

rsc.li/pccp

1. Introduction

After CH₃NH₃PbI₃ (MAPbI₃) was first used in photovoltaic solar cells obtaining a 3.8% efficiency,^{1,2} MAPbI₃ was considered as a potential material due to its wide electron and hole diffusion length, adjustable optical bandgap, high carrier mobility, high light absorption coefficient, and low production cost.^{3–8} In contrast to the slow development of silicon cells, the efficiency of perovskite solar cells has reached 25.7% in the last decade,^{9–11} which is comparable to that of single-crystal silicon materials.¹² Although the rapid development of MAPbI₃ in the last decade is desirable for photovoltaics, a stable operation for 25 years hinders its practical applications.^{13–15}

The stability of perovskite solar cells (PSCs) is a big challenge at present. During the stable operation of MAPbI₃ PSCs,

water and oxygen react with MAPbI₃, ultimately decreasing the lifespan of PSCs with reaction rates accelerating further in their combined presence.^{16,17} The usage of MAPbI₃ in good packaging materials can offer some respite in this regard. The temperature range for PSCs during operation is 60–85 °C.¹⁸ If the operating temperature surpasses this range, a significant amount of heat may be generated, leading to the decomposition of PSCs.^{19,20} Furthermore, high temperature leads to the decomposition of some packaging materials, which lowers the ultimate efficacy of MAPbI₃.²¹ It is imperative that we grasp the ins and outs of the decomposition mechanism of MAPbI₃.

Recently, several studies have offered insights into the decomposition mechanism of MAPbI₃. Conings *et al.*²² conducted a comprehensive investigation of MAPbI₃ under various conditions, discovering that heating MAPbI₃ to 358 K causes the PSCs to rupture with PbI₂ as a solid-state decomposition product. However, there is limited information about the gaseous decomposition product, which is critical for optimal synthetic conditions and annealing of the MAPbI₃ film.^{23,24} To fill in this critical gap, Dualeh *et al.*²⁵ mixed perovskite precursor solutions with varying proportions and subjected the resulting perovskite to heat treatment, producing HI and CH₃NH₂. This result is then supported by Philippe and Nenon.^{26,27} However, there have been inconsistent findings in the literature regarding the decomposition products. Williams *et al.*²⁸ utilized Fourier infrared (FTIR) spectroscopy to scrutinize the thermal decomposition process, revealing the characteristic peaks of NH₃ and CH₃I at 265 °C but no characteristic peaks of CH₃CH₂ and HI, which are aligned with previous

^a Department of Power Engineering, North China Electric Power University, Baoding 071003, Hebei, China. E-mail: gaozhyan@163.com

^b Hebei Key Laboratory of Low Carbon and High-Efficiency Power Generation Technology, North China Electric Power University, Baoding 071003, Hebei, China

^c Baoding Key Laboratory of Low Carbon and High-Efficiency Power Generation Technology, North China Electric Power University, Baoding 071003, Hebei, China

^d Institute of Clusters and Low Dimensional Nanomaterials, School of Mathematics and Physics, North China Electric Power University, Beijing 102206, P. R. China

^e Hebei Key Laboratory of Physics and Energy Technology, North China Electric Power University, Baoding 071000, Hebei, P. R. China

^f Advanced Institute for Materials Research (WPI-AIMR), Tohoku University, Sendai 980–8577, Japan. E-mail: li.hao.b8@tohoku.ac.jp

† Electronic supplementary information (ESI) available. See DOI: <https://doi.org/10.1039/d4cp01318b>

conclusions.^{24,29,30} Nonetheless, the conflicting research findings highlight the research limitations on the thermal decomposition reaction and products in perovskite, which fail to explore the stability of different crystal planes of MAPbI₃. There are still mysteries about the decomposition mechanism of MAPbI₃.

Motivated by the recent developments, this study analyzes the decomposition mechanism of MAPbI₃ through a combination of experiments and density functional theory (DFT) calculations. First, thermal gravimetric analysis (TGA) – FTIR reveals that MAPbI₃ decomposes into CH₃I, NH₃, and PbI₂, with two stages of decomposition distinguished: gas overflow (513–693 K) and solid sublimation (693–873 K). To assess the stability of various crystal surfaces of MAPbI₃, we conducted *in situ* X-ray diffraction (XRD), displaying conspicuous decomposition of (110), (220), and (310) surfaces between 550 and 600 K. To probe the stability of these three surfaces, we performed *ab initio* molecular dynamics (AIMD) simulations, mean square displacement (MSD), and XRD culminating for the most stable (220) surface. Moreover, the reaction energy barriers for the decomposition processes of (110) and (310) surfaces were calculated to be 2.07 and 2.88 eV, respectively. This work provides unique insights into the thermal decomposition mechanism of MAPbI₃, facilitating the development of stable and efficient PSCs.

2. Methods

2.1 Experimental method

Materials. The purity of the MAPbI₃ in this work (chemical abstracts service number: 69507-98-8) was 99%. These MAPbI₃ materials were obtained from McLean reagent company (China), and sealed in a dark brown reagent bottle in a nitrogen environment. All chemicals were used as-received without further purification unless otherwise stated.

Instrumental analysis. The S-4700 scanning electron microscope (SEM) produced by the HITACHI Company of Japan was used for this experimental observation. TGA measurements were carried out using a German-made thermal gravimetric analyzer, model NETZSCH TG 449-F5. The FTIR spectra of the evolved gases were simultaneously recorded with an FTIR spectrometer model STA449F5-INVENIO-R. The DSC experiments were performed on a synchrotron thermal analyzer STA449-F5 from NETZSCH, Germany. The thermal analysis was performed by heating the sample powder in an Al₂O₃ crucible from room temperature (27 °C) to 800 °C at a constant rate of 5, 10, and 20 °C min⁻¹, respectively. A flow rate of 50 ml min⁻¹ of N₂ was used as a delivery gas to create an inert atmosphere. *In situ* XRD patterns of MAPbI₃ powders were produced using a Panalytical model manufactured by Panacol in the Netherlands, with Cu K α irradiation of 1.54 Å at 40 kV and 40 mA, and the scanning range in the experiment was 5° to 90° with the scanning rate of 5° min⁻¹. The stepscan mode was used during the XRD analysis with a step size of 0.02°.

2.2 Computational methods

In this work, all DFT calculations were performed using the Vienna *ab initio* simulation package (VASP 5.4.4).^{31,32} The Perdew–Burke–Ernzerhof (PBE) functional with the generalized gradient approximation (GGA) and the projector-augmented wave (PAW) basis were used in the calculations.³³ We built the model with a vacuum layer of 20 Å in the z-direction and employed dipole corrections to eliminate the influence of the dipole distance. The energy cutoff of the plane wave basis was set equal to 520 eV and the value of the number of data points (NEDOS) was set to 1000. The force on each atom was set to be below 0.02 eV Å⁻¹ and the energy on each atom was set to be below 10⁻⁵ eV, as two necessary thresholds to stop structure optimization. To optimize the structures more accurately, the van der Waals interactions were considered in the calculations using the DFT-D3 method.³⁴

During AIMD simulations, we set the convergence standard of energy to 10⁻⁴ considering time and accuracy. AIMD was performed at 300 and 800 K to confirm the thermal stability of MAPbI₃ (110), (220), and (310). To ensure the precision of the thermal stability analysis, mean square displacement (MSD) was employed for validation. To obtain an accurate transition state, both climbing-image nudged elastic band (CI-NEB)^{35,36} and improved dimer method (IDM)³⁷ were employed. More specifically, the CI-NEB method was applied to roughly locate the structure in the transition state with a force convergence of 0.3 eV Å⁻¹, and the energy on each atom was set to be below 10⁻⁵ eV with a *k*-point of 1 × 1 × 1. Then, the IDM method was applied to accurately locate the structure in the transition state with a force convergence criterion of 0.05 eV Å⁻¹. The equation of reaction energy barrier (*G*_b) is shown in the ESI† (eqn (S1) and (S2))

3 Results and discussion

3.1 Experiments

The as-prepared MAPbI₃ powders demonstrate good crystallinities, as shown in Fig. 1a and b. The SEM morphology reveals that the methyl ammonium lead perovskite employed in this experiment was primarily composed of small particles, some of which adhered to form a larger rod-shaped structure that was advantageous for the follow-up thermal decomposition studies. Fig. 1c and d shows the results of heating MAPbI₃ from room temperature to 800 °C using the heating rates of 5, 10, and 20 °C min⁻¹. The generated gases were analyzed using TGA trace and FTIR spectra. The thermal decomposition of MAPbI₃ appeared to have two distinct stages as shown in Fig. 1c. The first stage occurred between 240 and 420 °C, with a 26% mass loss, which was consistent with earlier research.²⁹ The second stage occurred at between 420 and 600 °C, with a nearly 100% mass loss. The residual mass value of the first stage was equal to the relative molecular weight ratio of PbI₂ in MAPbI₃ (74.4%). We concluded that the first stage involved gas production while the second involved PbI₂ sublimation. The rate of TGA trials was demonstrated using its first derivative, and each curve

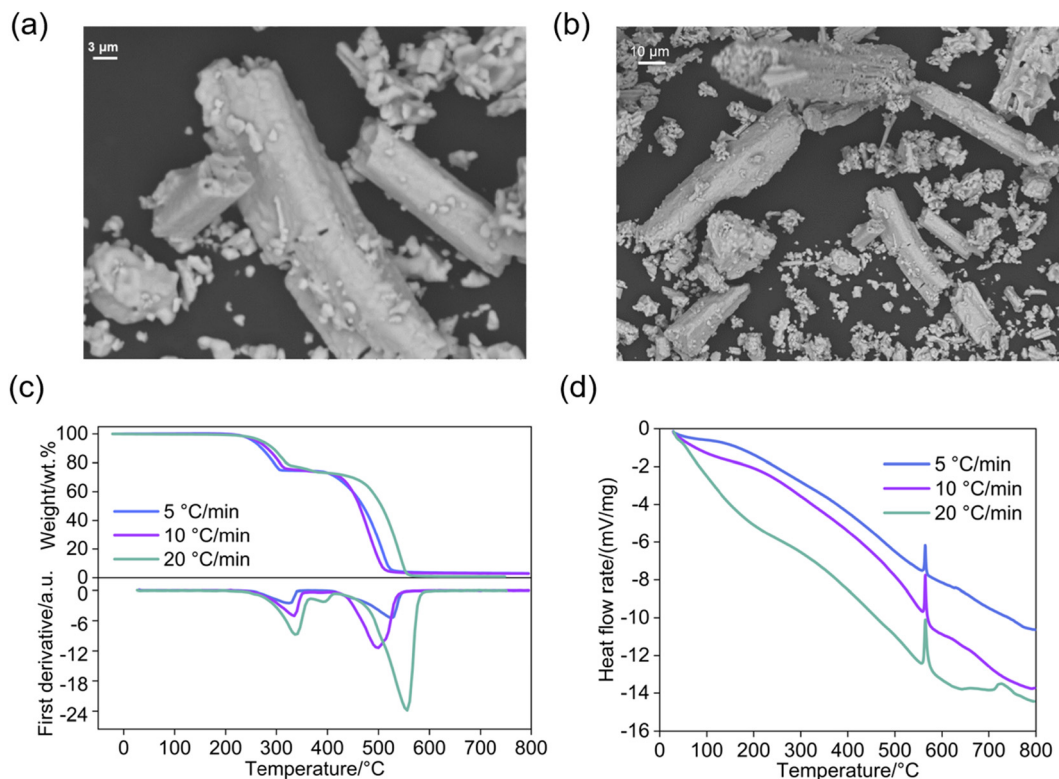


Fig. 1 (a) and (b) SEM of MAPbI₃; (c) TGA and the first derivative of TGA curves; (d) TGA-DSC curve.

contained two peaks. Increasing the heating rate raised the reaction rate, indicating that the reaction rate of the second stage was considerably higher than the first stage. We observed a delayed reaction during the thermal decomposition reaction due to the quick rise in the system temperature, which caused the reaction to occur at higher temperatures at faster heating rates. Furthermore, unlike the exothermic reaction of the thermal decomposition of ammonium perchlorate-based molecular perovskite,³⁸ the thermal decomposition of MAPbI₃ was heat-absorbing as shown in Fig. 1d, and the crystals showed no phase change during the early stage of thermal decomposition. However, a heat absorption peak emerged at approximately 564 °C, likely attributed to the melting of the PbI₂ solid.

To understand the gaseous products generated during the thermal decomposition stage, we simultaneously recorded the FTIR spectra of the escaping gas during TGA, as shown in Fig. 2. As the temperature rises, Fig. 2a–c shows the diffraction peaks of the thermal decomposition products. In this study, we focused on the spectral information at wavenumbers of 966, 1266, and 3016 cm⁻¹, which correspond to the characteristic peaks of the NH₃, CH₃I, and CH₄ groups. The fluctuations of the diffraction peaks were observed at the main reaction temperature, ranging from 270 to 480 °C, as shown in Fig. 2d–f. Our research showed that NH₃ and CH₃I were prominently visible at three heating rates and were likely among the products of the first stage. However, no evidence of a diffraction peak was found under 2229 (HI characteristic peak) and 2960 cm⁻¹ (CH₃NH₃I characteristic peak). It reveals

that the thermal decomposition gases of MAPbI₃ are NH₃ and CH₃I, instead of HI and CH₃NH₃I. This is in agreement with the findings of Williams *et al.*²⁸ Furthermore, findings from Juarez-Perez and Ciccioli *et al.* suggest that the nature of gaseous byproducts may vary depending on the experimental conditions employed.^{39,40} At a heating rate of 20 °C min⁻¹, the TGA curves demonstrated a distinct reaction mechanism occurring between 380 and 450 °C, which did not occur at the other two heating rates. This behavior is believed to be related to the creation of CH₄ in this area, based on the observation of FTIR spectra. Note that the peak temperature of CH₄ in the FTIR spectrum was considerably higher than those of NH₃ and CH₃I, indicating that CH₄ formed later than NH₃ and CH₃I. A hysteresis in the reaction was observed with increasing heating rates, which was consistent with the TGA tests. Furthermore, the diffraction peaks corresponding to the three products shifted towards higher temperatures with increase in the heating rate.

To explore the thermal decomposition process of perovskite, we conducted the *in situ* XRD of MAPbI₃ at different temperatures (300 to 700 K, Fig. 3). For higher accuracy, the measurements were performed in a nitrogen-only environment. At 300 K, the typical tetragonal MAPbI₃ perovskite diffraction peaks at 13.98° (110), 28.35° (220), and 31.74° (310) were present. These peaks are the characteristics of the tetragonal MAPbI₃ perovskite, indicating that the crystal purity of the experiments was reliable. Throughout the temperature range from 300 to 550 K, the diffraction peaks remained unaffected.⁴¹ However, at 600 K, the intensity of the diffraction peaks corresponding to the three

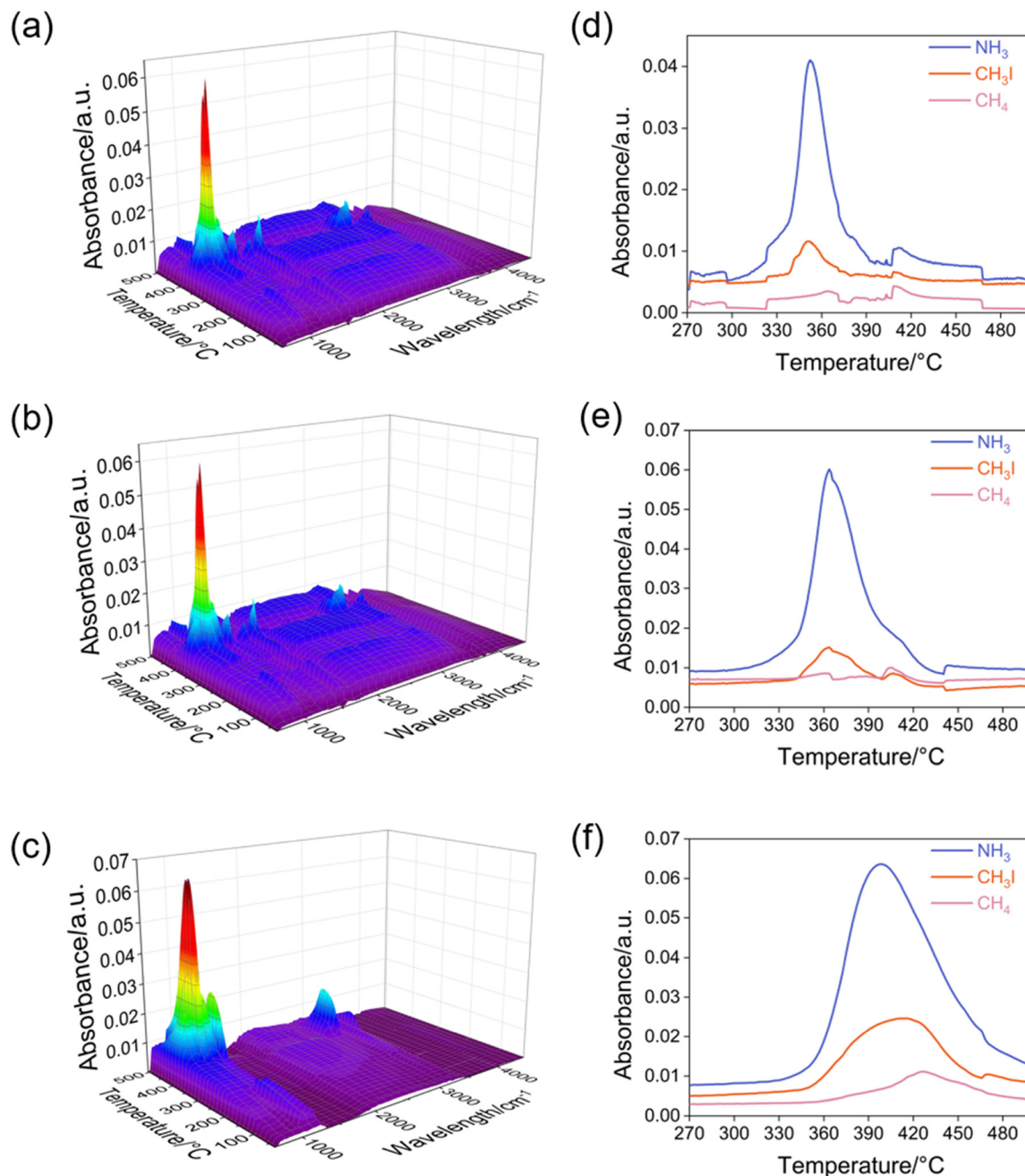


Fig. 2 (a) and (b) show the TG-FTIR spectra and product peaks at $5\text{ }^{\circ}\text{C min}^{-1}$; (b) and (e) show the TG-FTIR spectra and product peaks at $10\text{ }^{\circ}\text{C min}^{-1}$; (c) and (f) show the TG-FTIR spectra and product peaks at $20\text{ }^{\circ}\text{C min}^{-1}$.

classical characteristic crystal planes abruptly decreased. New peaks emerged at approximately 12.5° , 25.5° , and 39° , resembling the powder diffraction pattern of PbI_2 (PDF#07-0235).⁴² This indicated that MAPbI_3 starts to decompose at temperatures from 550 to 600 K, which was consistent with the results of the TG experiments above. The solid-phase product produced was PbI_2 .

3.2 DFT calculations

The aforementioned investigations have revealed key thermal decomposition byproducts of MAPbI_3 , namely NH_3 , CH_3I , and

PbI_2 , as the temperature increases. The degradation of MAPbI_3 specifically occurs on the (110), (220), and (310) surfaces, as indicated by our research. To assess its stability, we developed models based on these surfaces and performed AIMD simulations. To ensure accurate results, we maintained a thickness of 20 \AA in the z -direction and employed a multilayer model to preserve the ontological qualities of MAPbI_3 . Fig. S1a–c shows the front views of crystal surfaces, which were allowed to fully relax rather than having their atoms fixed. This ensured the high accuracy of our simulations. Each simulation supercell contained around 100 atoms.

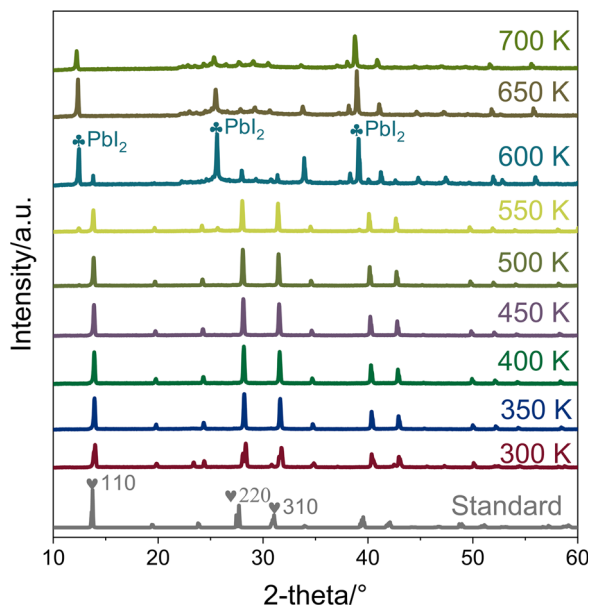


Fig. 3 The *in situ* XRD results of MAPbI₃.

To confirm the stabilities of the three surfaces, AIMD simulations were conducted from 300 to 800 K with the canonical ensemble (NVT) with a time step of 1.0 fs, together with the Nose thermostat (Fig. S2, ESI[†]).⁴³ The total simulation time was 6 ps. The range of energy fluctuations steadily widens with rising temperature, suggesting that MAPbI₃ becomes increasingly destabilized. The energy of the system is not constant but fluctuates over time.

To explore the stability, MSD was calculated as shown in Fig. 4a.^{44,45} Since MAPbI₃ is a framework composed of lead and iodine,^{46,47} herein, we investigated the diffusion of lead. As depicted in Fig. 4a, the MSD values for the three surfaces are remarkable, suggesting their stability at 300 K. However, as temperature escalates to 600 K, MSD values experience a significant rise on the (110) and (310) surfaces, while the MSD values on the (220) surface exhibit relatively minimal change. This indicates that the stability of the (110) and (310) surfaces is not as robust as (220) when subjected to heating processes. Furthermore, our study also involved the calculation of XRD for the initial and final states of the three surfaces, as shown in Fig. 4b. The results show that our calculated XRD is consistent with the experimental *in situ* XRD. Fig. S3–S5 (ESI[†]) show that the diffraction peaks of the (110), (220), and (310) surfaces have decreased to varying degrees at 600 K, signifying the decomposition of the crystal surfaces, as suggested by our experimental observations. Interestingly, the diffraction peaks on the (220) surface illustrate the least reduction compared to the other two surfaces, as shown in Table 1, further validating that the surface of (220) is the most stable among the three surfaces, which is consistent with our aforementioned MSD findings.

Based on our analyses above, we have found that the (110) and (310) surfaces experience significant stability changes during heating. Therefore, this study will further delve into

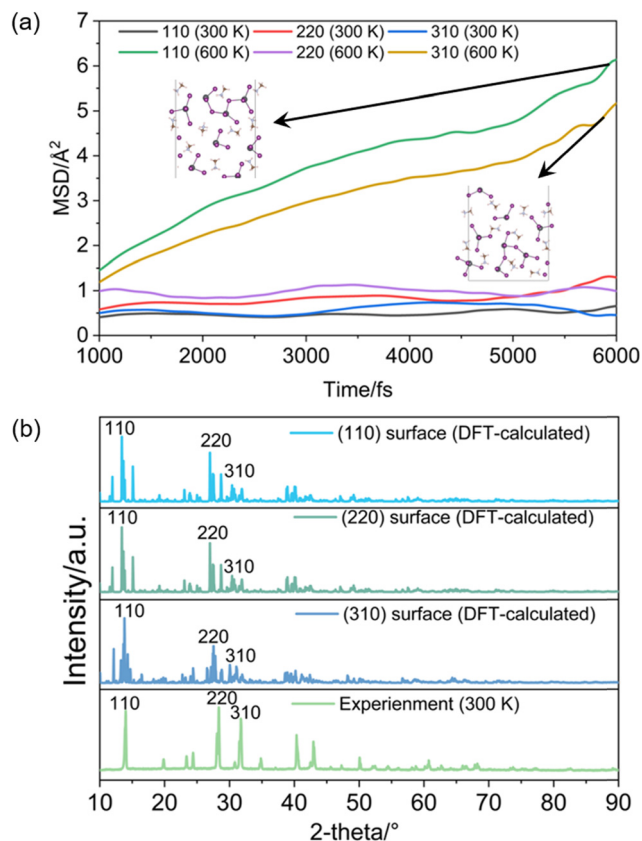


Fig. 4 (a) MSD of MAPbI₃ at 300 K; (b) comparison between the experimental and DFT-calculated XRD results.

Table 1 Percentage of diffraction decomposition on different surfaces

	110 surface	220 surface	310 surface
110 diffraction peak (a.u.)	50.73	53.23	37.97
220 diffraction peak (a.u.)	0	31.37	26.42
310 diffraction peak (a.u.)	44.31	34.97	34.23

the decomposition of these two surfaces. Our experiments reveal that the thermal decomposition of MAPbI₃ generates CH₃I, NH₃, and PbI₂. To gain a deeper understanding of the thermal decomposition process, we employed transition state calculations on both surfaces. The transition state of the (110) surface is illustrated in Fig. 5, demonstrating that the cleavage of CH₃ and NH₃ occurs at 600 K. This is promptly followed by the combination of CH₃ and iodine ions, resulting in the formation of CH₃I. The reaction energy barrier for this process of the (110) surface is 2.07 eV, while that for the (310) surface is 2.88 eV (Fig. 5). Reaction energy barriers for these two surfaces are > 2 eV, implying that these two surfaces do not spontaneously form at room temperature. Furthermore, the reaction energy barrier of the (310) surface is 0.71 eV, which is greater than that of (110). This suggests that (310) is more stable than (110), reinforcing the conclusion obtained from our MSD analyses.

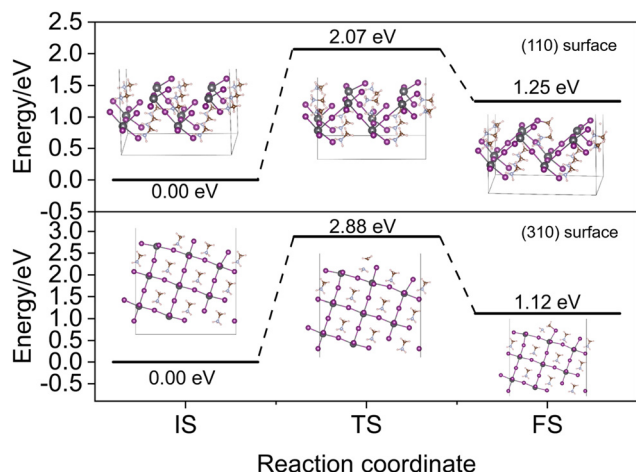


Fig. 5 Reaction energy diagrams showing the initial, transition, and final states (IS, TS, and FS, respectively) of MAPbI₃ thermal decomposition.

4. Conclusion

To summarize, we have utilized TGA-FTIR technology to illuminate the thermal decomposition process of MAPbI₃. Through experimentation, we determined that CH₃I, NH₃, and PbI₂ are the thermal decomposition products of MAPbI₃, with MA ions decomposing at 513 K and solid decomposition occurring at a minimum of 693 K. Prolonged exposure to heat can result in delayed reactions and sufficient time is required for MAPbI₃ decomposition. Importantly, our *in situ* XRD analysis revealed that the (110), (220), and (310) surfaces of MAPbI₃ will experience significant decomposition at the temperature between 550 and 600 K, generating PbI₂. The subsequent MSD calculations discovered that the (220) surface is the most stable among the three surfaces. In addition, our XRD analysis showed a reduction in diffraction peaks for all three crystal surfaces; however, the (220) surface with the least reduction highlighted the superior stability of the (220) surface. Furthermore, we simulated the thermal decomposition of (110) and (310), resulting in the reaction energy barriers of 2.07 and 2.88 eV, respectively. This suggests that neither of these surfaces can decompose spontaneously at room temperature, and the (310) surface is more stable than the (110) surface. These findings provide new insights into the thermal stability and degradation mechanism of MAPbI₃ and offer theoretical support for enhancing the perovskite-based stability of devices.

Author contributions

Zhengyang Gao, Hao Li, Xunlei Ding, and Weijie Yang conceived and supervised the project. Zhengyang Gao corrected the writing of the manuscript, guided the manuscript throughout the writing process, and the structure construction of the paper, the relevant theoretical support, and the research subject and ideas of the paper. Huan Lu, Kailong Liu, and Ruiyang Shi wrote the first draft of the thesis, completed the revision of the thesis under the supervisor's guidance, and completed the

calculation of the thesis results and graphical plotting work. Yang Bai and Qingqi Yan provide the relevant research data for the thesis. Weijie Yang participated in the revision of the manuscript, verified the thesis, and carefully reviewed the results of each part of the paper. Xunlei Ding participated in the correction of the manuscript. All authors discussed the results.

Conflicts of interest

There are no conflicts to declare.

Acknowledgements

This work was financially supported by the National Natural Science Foundation of China (92161115, 61704054), and the Fundamental Research Fund for the Central Universities (2023MS125). The work was also supported by the Natural Science Foundation of Hebei (No.E2023502006) and Beijing Natural Science Foundation (No. 2214064). We acknowledge the Center for Computational Materials Science, Institute for Materials Research, Tohoku University for the use of MASAMUNE-IMR (No. 202212-SCKXX-0204), and the Institute for Solid State Physics (ISSP) at the University of Tokyo for the use of their supercomputers. The authors also acknowledge Beijing PARATERA Tech Co., Ltd. for providing HPC resources.

References

- 1 A. Kojima, K. Teshima, Y. Shirai and T. Miyasaka, *J. Am. Chem. Soc.*, 2009, **131**, 6050–6051.
- 2 Y. Xie, D. Chen, T. Chen, T. Zhang, Y. Yin and X. Qiu, *Mater. Sci. Semicond. Process.*, 2023, **168**, 107853.
- 3 M. Azam, S. Yue, R. Xu, K. Liu, K. Ren, Y. Sun, J. Liu, Z. Wang, S. Qu, Y. Lei and Z. Wang, *J. Mater. Chem. A*, 2018, **6**, 13725–13734.
- 4 C. C. Stoumpos, C. D. Malliakas and M. G. Kanatzidis, *Inorg. Chem.*, 2013, **52**, 9019–9038.
- 5 S. D. Stranks, G. E. Eperon, G. Grancini, C. Menelaou, M. J. P. Alcocer, T. Leijtens, L. M. Herz, A. Petrozza and H. J. Snaith, *Science*, 2013, **342**, 341–344.
- 6 W. J. Yin, T. Shi and Y. Yan, *Adv. Mater.*, 2014, **26**, 4653–4658.
- 7 D. B. Mitzi, *Prog. Inorg. Chem.*, 1999, 1–121.
- 8 Y. Chen, X. Ding, L. Yang, Y. Wang, J. I. Gurti, M. Wang, W. Li, X. Wang and W. Yang, *Phys. Chem. Chem. Phys.*, 2022, **24**, 14375–14389.
- 9 K. Jung, W.-S. Chae, Y. C. Park, J. Kim and M.-J. Lee, *Chem. Eng. J.*, 2020, **380**, 122436.
- 10 Y. Hou, E. Aydin, M. De Bastiani, C. Xiao, F. H. Isikgor, D.-J. Xue, B. Chen, H. Chen, B. Bahrami, A. H. Chowdhury, A. Johnston, S.-W. Baek, Z. Huang, M. Wei, Y. Dong, J. Troughton, R. Jalmoood, A. J. Mirabelli, T. G. Allen, E. Van Kerschaver, M. I. Saidaminov, D. Baran, Q. Qiao,

- K. Zhu, S. De Wolf and E. H. Sargent, *Science*, 2020, **367**, 1135–1140.
- 11 N. K. Elangovan, R. Kannadasan, M. F. Savio, S. Vinson Joshua and M. Faheem, *Energy Sci. Eng.*, 2024, **12**(5), 2004–2016.
- 12 Z. Gao, Y. Bai, M. Wang, G. Mao, X. Liu, P. Gao, W. Yang, X. Ding and J. Yao, *J. Phys. Chem. C*, 2022, **126**, 13409–13415.
- 13 D. C. Miller, H. I. Khonkar, R. Herrero, I. Antón, D. K. Johnson, T. Hornung, T. Schmid-Schirling, T. B. Vinzant, S. Deutch, B. To, G. Sala and S. R. Kurtz, *Solar Energy Mater. Solar Cells*, 2017, **167**, 7–21.
- 14 V. Arjun, K. P. Muthukumaran, A. Nithya, M. Yoshimura and S. Karuppuchamy, *Solar Energy Mater. Solar Cells*, 2024, **271**, 112857.
- 15 E. M. Mkawi, S. M. H. Qaid, E. Bekyarova and A. S. Aldwayyan, *Opt. Mater.*, 2024, **152**, 115473.
- 16 J. Zhao, B. Cai, Z. Luo, Y. Dong, Y. Zhang, H. Xu, B. Hong, Y. Yang, L. Li, W. Zhang and C. Gao, *Sci. Rep.*, 2016, **6**, 21976.
- 17 L. Zhang and P. H. L. Sit, *J. Mater. Chem. A*, 2017, **5**, 9042–9049.
- 18 L. Liu, B. Farhadi, J. Li, S. Liu, L. Lu, H. Wang, M. Du, L. Yang, S. Bao, X. Jiang, X. Dong, Q. Miao, D. Li, K. Wang and S. F. Liu, *Angew. Chem., Int. Ed.*, 2024, **63**, e202317972.
- 19 A. Dualeh, N. Tétreault, T. Moehl, P. Gao, M. K. Nazeeruddin and M. Grätzel, *Adv. Funct. Mater.*, 2014, **24**, 3250–3258.
- 20 T. Supasai, N. Rujisamphan, K. Ullrich, A. Chemseddine and T. Dittrich, *Appl. Phys. Lett.*, 2013, **103**, 183906.
- 21 T. Burwig, K. Heinze and P. Pistor, *Phys. Rev. Mater.*, 2022, **6**, 065404.
- 22 B. Conings, J. Drijkoningen, N. Gauquelin, A. Babayigit, J. D'Haen, L. D'Olieslaeger, A. Ethirajan, J. Verbeeck, J. Manca, E. Mosconi, F. D. Angelis and H.-G. Boyen, *Adv. Energy Mater.*, 2015, **5**, 1500477.
- 23 Z. Song, S. C. Wathage, A. B. Phillips, B. L. Tompkins, R. J. Ellingson and M. J. Heben, *Chem. Mater.*, 2015, **27**, 4612–4619.
- 24 A. Latini, G. Gigli and A. Ciccioli, *Sustainable Energy Fuels*, 2017, **1**, 1351–1357.
- 25 A. Dualeh, P. Gao, S. I. Seok, M. K. Nazeeruddin and M. Grätzel, *Chem. Mater.*, 2014, **26**, 6160–6164.
- 26 B. Philippe, B.-W. Park, R. Lindblad, J. Oscarsson, S. Ahmadi, E. M. J. Johansson and H. Rensmo, *Chem. Mater.*, 2015, **27**, 1720–1731.
- 27 D. P. Nenon, J. A. Christians, L. M. Wheeler, J. L. Blackburn, E. M. Sanehira, B. Dou, M. L. Olsen, K. Zhu, J. J. Berry and J. M. Luther, *Energy Environ. Sci.*, 2016, **9**, 2072–2082.
- 28 A. E. Williams, P. J. Holliman, M. J. Carnie, M. L. Davies, D. A. Worsley and T. M. Watson, *J. Mater. Chem. A*, 2014, **2**, 19338–19346.
- 29 L. Ma, D. Guo, M. Li, C. Wang, Z. Zhou, X. Zhao, F. Zhang, Z. Ao and Z. Nie, *Chem. Mater.*, 2019, **31**, 8515–8522.
- 30 E. J. Juarez-Perez, Z. Hawash, S. R. Raga, L. K. Ono and Y. Qi, *Energy Environ. Sci.*, 2016, **9**, 3406–3410.
- 31 G. Kresse and J. Furthmüller, *Phys. Rev. B: Solid State*, 1996, **54**, 11169–11186.
- 32 G. Kresse and J. Furthmüller, *Comput. Mater. Sci.*, 1996, **6**, 15–50.
- 33 J. P. Perdew, K. Burke and M. Ernzerhof, *Phys. Rev. Lett.*, 1996, **77**, 3865–3868.
- 34 S. Grimme, J. Antony, S. Ehrlich and H. Krieg, *J. Chem. Phys.*, 2010, **132**, 154104.
- 35 G. Henkelman, B. P. Uberuaga and H. Jónsson, *J. Chem. Phys.*, 2000, **113**, 9901–9904.
- 36 G. Henkelman and H. Jónsson, *J. Chem. Phys.*, 2000, **113**, 9978–9985.
- 37 A. Heyden, A. T. Bell and F. J. Keil, *J. Chem. Phys.*, 2005, **123**, 224101.
- 38 P. Zhai, C. Shi, S. Zhao, W. Liu, W. Wang and L. Yao, *RSC Adv.*, 2021, **11**, 16388–16395.
- 39 E. J. Juarez-Perez, L. K. Ono, I. Uriarte, E. J. Cocinero and Y. Qi, *ACS Appl. Mater. Interfaces*, 2019, **11**, 12586–12593.
- 40 A. Ciccioli and A. Latini, *J. Phys. Chem. Lett.*, 2018, **9**, 3756–3765.
- 41 J. Han, Z. Liang, S. Guo, S. Wang and S. Qiao, *Surfaces Interfaces*, 2022, **34**, 102315.
- 42 J. Zhao, B. Cai, Z. Luo, Y. Dong, Y. Zhang, H. Xu, B. Hong, Y. Yang, L. Li, W. Zhang and C. Gao, *Sci. Rep.*, 2016, **6**, 21976.
- 43 Z. Gao, M. Wang, H. Zhang, S. Chen, C. Wu, I. D. Gates, W. Yang, X. Ding and J. Yao, *Solar Energy Mater. Solar Cells*, 2021, **233**, 111401.
- 44 Z. Gao, H. Zhang, G. Mao, J. Ren, Z. Chen, C. Wu, I. D. Gates, W. Yang, X. Ding and J. Yao, *Appl. Surf. Sci.*, 2021, **568**, 150916.
- 45 L. Yang, Y. Chen, X. Wang, J. Deng, W. Wang, X. Ding, W. Yang and J. Yao, *J. Phys. Chem. C*, 2021, **125**, 24096–24104.
- 46 M. Faghihnasiri, M. Izadifard and M. E. Ghazi, *J. Phys. Chem. C*, 2017, **121**, 27059–27070.
- 47 S. Nachimuthu, M.-Q. Cai, Y.-C. Wang, S.-H. Xu, L.-Y. Chen and J.-C. Jiang, *Mater. Today Adv.*, 2023, **18**, 100370.